Additive-Free Crystallization Modulation for Efficient Perovskite Solar Cells by a Transverse Pulsed Electric Field

Hai-Fang Li, Pengkun Zhu, Zhiyu Zhang, Xin Sun, Shuailin Chen, Teng Xu, Bingbing Fan, Peng Cui, Liang Li, Lihua Chu, and Meicheng Li*

Controlling the migration and spatial distribution of ionic constituents during perovskite growth represents a powerful approach to modulate the crystallization process and achieve optimal film morphology. However, the well-controlled regulation of specific ionic species and its consequences for oriented growth and defect suppression have received limited attention. Herein, a transverse pulsed electric field (e-field) is introduced to guide the directional migration of perovskite constituents, offering an alternative to crystallization control that is typically achieved with chemical additives. The MAPbI$_3$ (where MA$^+$ is CH$_3$NH$_3$$^+$) films exhibit a lateral gradient in iodine species distribution, which correlates with improved crystal orientation, decreased iodide loss, and reduced formation of iodide vacancies. The e-field-assisted thermal annealing enables the facile migration of unanchored iodides in perovskite films, allowing mobile I$^-$ ions to fill vacancies and passivate undercoordinated Pb^{2+} sites. This e-field-driven ion migration and self-filling of iodide vacancies in MAPbI$_3$ could mitigate iodine-related defects caused by iodine loss and lower non-radiative recombination, leading to perovskite solar cells with improved efficiency and stability. Furthermore, this strategy is adaptable to the perovskites with mixed A-site cations and halides, delivering an efficiency of over 24%. These results provide new insights into defect self-passivation mediated with controlled e-field for high-performance devices.

1. Introduction

Metal halide perovskite solar cells (PSCs) have garnered extensive research attention as promising candidates for thin-film photovoltaic technologies.[1,2] The last decade has witnessed remarkable progress in power conversion efficiencies (PCEs) of single-junction PSCs exceeding 26%,[3,4] which capitalize on the numerous superior optoelectronic properties of perovskites, including tunable bandgap, low-energy exciton binding, and long-range carrier diffusion.[5] Advancing fabrication method for achieving high-performance perovskite absorbers has been a long-standing concern. To date, solution processing is extensively utilized to prepare perovskite films due to the compatibility with perovskite precursors and the ability of finely regulating the solution properties via solvent tuning and additive incorporation.[6] However, the solution-processed perovskite films often suffer from fast crystallization, resulting in the poor morphology of polycrystalline films with abundant grain boundaries from spin-coating deposition. Regulating the crystallization kinetics is therefore crucial in obtaining perovskites with improved crystallinity and film quality.[7] One promising approach involves the utilization of chemical additives, such as organic molecules,[8–10] polymers,[11] and organic halide salts[12–14] forming intermediate adducts with perovskite precursors to retard the perovskite nucleation/growth rates. Many of structural residues from additives incorporated into perovskite films, however, render a potential threat of instability caused by providing carrier recombination or degradation centers due to the heterogeneous microstructure. Thus, there is still the urgent need for an alternative approach capable of rational regulation of the crystallization kinetics in solution deposition of perovskite films to achieve stable and efficient PSCs.

External electric field (e-field) is widely used to controllably modulate the nucleation and growth kinetics of ionic crystals to obtain the required optoelectronic properties as a key activating element. Perovskite materials feature ionic constituents,[15] beneficial for the component migration and redistribution induced by external e-fields to regulate perovskite crystallization.[16,17] Therefore, employing controlled e-fields to modulate the nucleation/growth kinetics of perovskites offers a promising additive-free approach to improve the performance of perovskite films. A possibility of external e-field-assisted crystallization has been demonstrated during thermal annealing in a one-step process for perovskite films.[17,18] Controlling the ion polarization orientation by regulating ionic species migration in perovskite films along the applied external e-field was identified to facilitate the film crystallization and the built-in e-field enhancement.[17] Later,

H.-F. Li, P. Zhu, Z. Zhang, X. Sun, S. Chen, T. Xu, B. Fan, P. Cui, L. Li,
L. Chu, M. Li
State Key Laboratory of Alternate Electrical Power System with Renewable Energy Sources
School of New Energy
North China Electric Power University
Beijing 102206, China
E-mail: mcli@ncepu.edu.cn

**ADVANCED
SCIENCE NEWS**

www.advancedsciencenews.com

**small
methods**

www.small-methods.com

the external e-field was further expanded to the two-step solution to control the crystallization of perovskite films.[19] The improved crystallinity of perovskite films was characterized by relying on e-field to guide the organic cation migration (MA^+ and FA^+) for facilitating the reaction with PbI_2. Furthermore, an alternative external field was introduced by applying alternating e-field, instead of the electrostatic e-field studied above, on the intermediate state to modulate perovskite formation during the thermal annealing.[20] The morphology and microstructure of perovskite films were effectively regulated by the controlled motion of ionic species under tuning the amplitude and frequency of the e-field. These studies mainly focused on producing a uniformly dense and defect-less perovskite layer arising from the regulation of longitudinal species transport within film by applying e-field perpendicular to the perovskite surface. However, limited attention has been paid to transverse e-field parallel to perovskite surface, and the effect of transverse e-field on regulating the distribution of ionic species to the performance of perovskite film and the resulting device is far from clear.

In this study, a transverse pulsed e-field, parallel to the surface of perovskite film, was introduced as an additive-free strategy to modulate the crystallization dynamics of the perovskite crystals. Controlling the migration and distribution of the ionic species during the film formation is beneficial for the preparation of high-quality perovskite films without additive residues. The resulting perovskite films with the incorporation of pulsed e-field are found to be an existence of a lateral gradient distribution of iodine-related species, simultaneously demonstrating reduced loss of iodides during thermal annealing and suppressed formation of iodide vacancies. Unlike thermally induced disordering of ionic species when annealing perovskite films, which can cause morphology deterioration and halide migration and loss, the ordered migration and distribution of iodides achieved with pulsed e-field under combined heat stimuli. As a result, the pulsed e-field-assisted perovskite film showed enhanced film crystallinity, improved carrier transport, along with mitigated trap-state-related recombination relative to the untreated control film. An enhanced efficiency for the resulting PSCs was achieved, accompanied by extended environmental stability. Moreover, this strategy was also extended to the fabrication of high-quality mixed-cation and mixed-halide perovskite films. These insights regarding modulation of the migration and distribution of halide-related species during perovskite film formation contribute perspectives for developing efficient and stable perovskites in photovoltaics.

2. Results and Discussion

2.1. Evolution of Transverse Pulsed e-field on Perovskite Crystallization

Methylammonium lead iodide ($CH_3NH_3PbI_3$, $MAPbI_3$) was employed to study the crystallization modulation induced by transverse e-field for the fabrication of perovskite films. The $MAPbI_3$ films were prepared using a one-step spin-coating process. The external transverse pulsed e-field was applied on the spin-coated films under ambient conditions with a temperature of 23 ± 1 °C and a relative humidity (RH) of $35 \pm 2\%$ while thermal annealing was simultaneously conducted. The configuration of the

setup and the applied waveforms of the e-field were illustrated in **Figures** 1a and S1 (Supporting Information). Two opposite stainless-steel electrodes, which are at ≈0.7 mm from the side edge of perovskite film, were used to apply e-field for crystallization modulation of perovskite films. A pulsed e-field with a monopolar square-wave envelope (fixed 50% on-field signal) was applied to the the perovskite to induce lateral migration of ionic components along the field direction under bias.[21] Steady-state photoluminescence (PL) spectroscopy as a perovskite surface specific probe[22] was used to quickly evaluate the effects of the transverse e-field on the properties of the corresponding perovskite films. The e-field with direct-current (DC) waveform was also taken into account. The PL spectra demonstrated that the pulsed e-field-treated perovskite film has higher intensities compared to those with and without DC e-field treatments (Figure S2a, Supporting Information), which indicates that the perovskites film with pulsed e-field treatment greatly reduces the defect-assisted recombination process and non-radiative losses. These observations suggest that the thermal annealing of perovskites involving the crystallization modulation induced with the transverse pulsed e-field can facilitate the performance improvement of the resulting films. The frequency of the pulsed e-field is associated with the time scale for transport and distribution of ionic species in perovskites. Subsequently, the preferred frequency of the applied e-field was characterized to be 100 Hz (Figure S2b,c, Supporting Information), corresponding to the characteristic time scale of ion transport in perovskites.[23]

The steady-state PL studies of $MAPbI_3$ film treated with pulsed e-field at different magnitudes of the voltages were performed to identify the optimal driving force to ionic component migration in modulating the perovskite crystallization during thermal annealing. The optimized e-field was characterized with the field intensity of 17.5 V cm^{-1} (Figure S2d, Supporting Information). Additionally, X-ray diffraction (XRD) measurements were also performed to study the crystallinity of the perovskites films treated using a pulsed e-field with varied applied voltages (Figure 1b). Three strong diffraction peaks at 14.31, 28.64, and 32.07°, corresponding to the (110), (220), and (310) planes of the control perovskite film, respectively, were observed.[24] The as-prepared perovskite films with and without pulsed e-field treatment exhibited the same crystal structure and no peak shifting presented in the enlarged XRD patterns of the films (Figure S3a, Supporting Information), which indicates the same parallel atomic plane spacing in the pulsed e-field-treated perovskite films. These results demonstrate that the applied e-field does not lead to a lattice expansion/contraction of the resulting film.[25] Additionally, the e-field-treated perovskite film was cut into three parts along the direction of the e-field for XRD measurements (Figure S3b–d, Supporting Information). These is no significant shift in the observed (110), (220), and (310) diffraction peaks. This also means, in the pulsed e-field-assisted annealing process, that the distribution of the inorganic octahedral cages in the perovskite films does not change. With increase in the voltages applied during perovskite annealing, the intensity of the diffraction peak at the (110) plane gradually increased and showed a maximum for the perovskite film subjected to a pulsed e-field at an intensity of 17.5 V cm^{-1} (Figure 1b). Concurrently, the corresponding full width at half maximum (FWHM) exhibited a consistent decline, attaining a minimum for the perovskite film optimized with the
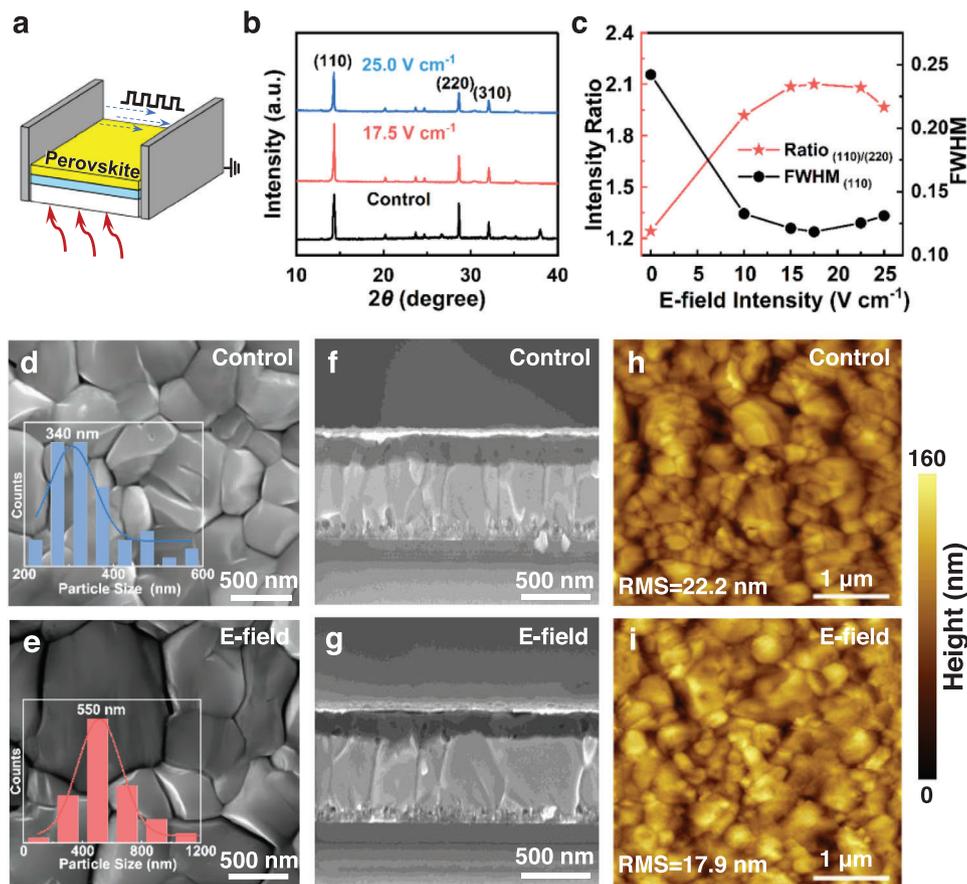
Figure 1. a) Schematic illustration of fabricating perovskite films with pulsed e-field-assisted crystallization regulation. b) XRD patterns of perovskite films without and with pulsed e-field treatment, and c) the corresponding FWHM of (110) facet and ratio of the intensity of (110)/(220) planes extracted from XRD patterns. SEM images of the top view for d) control and e) pulsed e-field-treated perovskite films. Cross-sectional SEM images of f) control and g) pulsed e-field-treated perovskite films. AFM images of perovskite films h) without and i) with pulsed e-field treatment. The statistical distributions of the average crystal size of the corresponding perovskite films were displayed in the insets of Figure 1d,e. The pulsed e-field applied to perovskite crystallization was 17.5 V cm^{-1} of field amplitude and a repetition rate of 100 Hz for duration time of 15 min.

same field intensity (Figure 1c). These results are attributed to an improvement in the crystallinity of perovskites with the pulsed e-field treatment. Moreover, the diffraction intensity of (110)/(220) peak in the modified perovskite film with pulsed e-field at 17.5 V cm^{-1} also increased by ≈1.7 times in comparison to the untreated control film (Figure 1c), demonstrating that the crystal growth direction is preferred along the (110) facet.[26] The increase in XRD intensity of the (110)/(220) peak may result from an increased density of coherent scattering from domains oriented in the [110] direction,[27] which may be attributed to fabrication conditions. The (110) orientation of the perovskite film is conducive to hole transfer from the perovskite to hole transport materials (HTMs), owing to the increased electrostatic potential and enhanced electronic cloud overlapping at the interface.[10] These results suggest that thermal annealing assisted with pulsed e-field promotes the crystallization and orientation of the resulting perovskite film.

Scanning electron microscopy (SEM) was carried out to study the effect of pulsed e-field treatment on the morphology of perovskite films. Top-view SEM images showed that the films modulated with and without pulsed e-field were covered fully by polycrystalline perovskites and exhibited compact surface morphol-

ogy (Figure 1d,e; Figure S4, Supporting Information). The grain size statistical distributions displayed that the average crystal size of the pulsed e-field-treated perovskite film was ≈550 nm, which was ≈210 nm larger than that of the control case (insets in Figure 1d,e). The increased grain size of the e-field-treated film could also be observed from the cross-sectional SEM images (Figure S4, Supporting Information). Compared to the control film with disordered crystal grains (Figure 1f), the pulsed e-field-treated perovskite film showed vertically penetrating crystals and reduced grain boundaries (Figure 1g). The results suggest that the crystal quality of the perovskite film is improved by pulsed e-field treatment, which is in good agreement with the XRD results. Besides, the improved film quality of pulsed e-field-treated films in comparison with the control film was further verified by the atomic force microscopy (AFM) measurements (Figure S5, Supporting Information). The root-mean-square (RMS) roughness of the e-field-treated perovskite film was 17.9 nm, apparently lower than that of the control film with RMS value of 22.2 nm (Figure 1h,i). The decreased roughness of perovskite film can be ascribed to the pulsed e-field that modulate the crystallization process of perovskite films though regulating
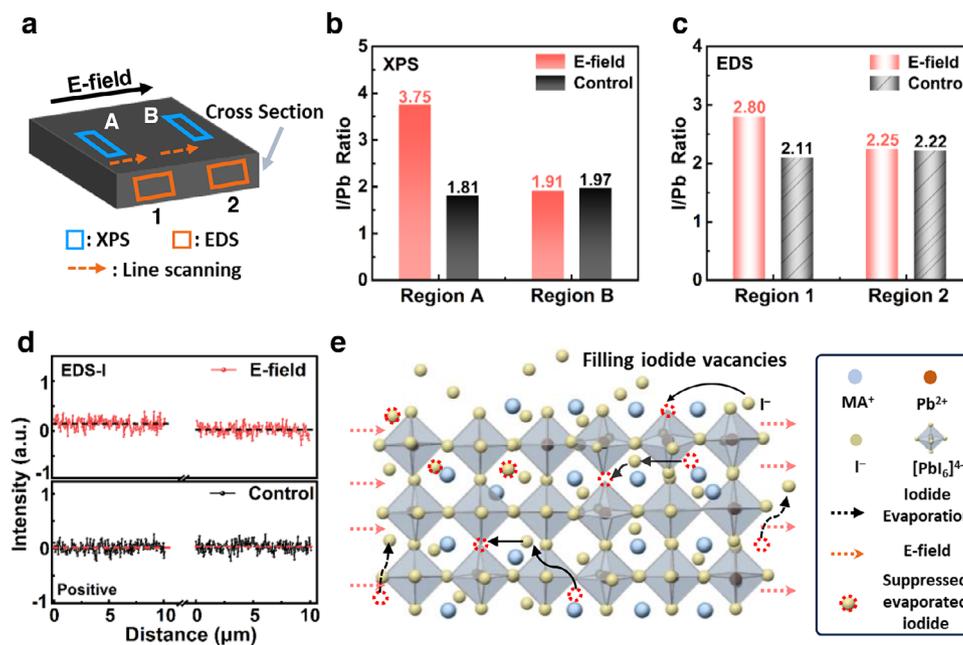
Figure 2. a) Schematic diagram of the areas analyzed with XPS and EDS measurements. b) I/Pb ratios at regions A and B on the perovskite surface with and without pulsed e-field treatment based on the data extracted from XPS. c) I/Pb ratios at regions 1 and 2 on the cross section of perovskite film treated with and without pulsed e-field from EDS measurement. d) Intensities of I element from EDS line-scanning of perovskite film with and without pulsed e-field treatment. The median line is defined by the middle value and highlighted. e) Schematic illustration of the effect mechanism for fabricating perovskite film with pulsed e-field treatment. Detailed information about the defined regions A, B and 1, 2 in panel a are given in Figure S7 (Supporting Information). The original XPS spectra of perovskite films with and without pulsed e-field treatment are given in Figure S8 (Supporting Information). The enlarged profiles of panel d can be found in Figure S9 (Supporting Information).

migration of ionic components, resulting in formation of a flat perovskite film. The flat perovskite film is beneficial to improving the contact between the perovskite layer and the HTMs. Moreover, the impact of pulsed e-field on the surface of perovskite was examined with contact angle tests. The water contact angle on the perovskite surface increased from 26.5 to 38.9° when the perovskite crystallization was modulated with the pulsed e-field (Figure S6, Supporting Information). With the introduction of pulsed e-field, the surface hydrophobicity of the perovskite films increased, attributing to the surface with compact perovskite grains, consist of more highly oriented crystals (Figure 1c).[28] These observations indicate that the introduction of pulsed e-field into the thermal annealing for crystallization and growth regulation could improve crystallinity, promote uniformity, and reduce surface roughness of the resultant perovskite films, thus beneficial for the deposition of uniform HTMs above perovskite layers.[29]

2.2. Interaction Between Pulsed e-field and Perovskite Films

X-ray photoelectron spectroscopy (XPS) was employed to investigate the surface characters of the perovskite film after introduction of the pulsed e-field. The two selected regions A and B along the e-field direction shown in **Figure 2a** clearly depicted that two dominant I 3d peaks at 618.51 eV (I $3d_{5/2}$) and 629.36 eV (I $3d_{3/2}$) were observed for the control film (Figure S8a, Supporting Information). There was no significant shift in the position of I 3d peaks for the modified films after the pulsed e-field treatment,

implying a uniform chemical environment for the I element in perovskite films with or without pulsed e-field treatment even in ambient condition. The Pb 4f spectra shown in Figure S8b (Supporting Information) gave similar results in terms of a negligible shift of Pb $4f_{7/2}$ and Pb $4f_{5/2}$ peaks after pulsed e-field introduction. The average I/Pb ratios for the perovskite film surfaces with or without pulsed e-field treatment were calculated from the integral area of the corresponding XPS peaks, and the results were shown in Figure 2b. The surface I/Pb ratio in region A of the e-field-free perovskite film was characterized to be ≈1.81, which is closer to the ratio detected in the region B adjacent to the opposite edge of the perovskite film (≈1.97), indicating a homogeneous structural composition across the surface of the control perovskite film. It is noteworthy that both I/Pb ratios in regions A and B is lower than the theoretical stoichiometric value close to 3 of a pure iodide-based perovskite.[30] For the pristine MAPbI$_3$, it was confirmed that the easy evaporation characteristic of organic halides (MAI) during thermal annealing would induce iodide deficiency in the neat perovskite film surface and thus stoichiometric I/Pb ratio below ≈3.[31] After the pulsed e-field treatment, the average I/Pb ratio at the perovskite surface showed a significant variation compared with the control film. Specifically, the I/Pb ratio at the surface of region A near the positive electrode substantially increased from ≈1.81 to ≈3.75 after applying a pulsed e-field to perovskite crystallization during thermal annealing, signifying the accumulation of I-related species. This observation shows that the surface area of modified perovskite adjacent to the positive electrode exhibited an I-rich condition (I/Pb ratio > 3), which should originate from the migration of surface

I⁻ ions controlled with the pulsed e-field. In contrast to notable I/Pb ratio increase in the region A of the perovskite film, these was a tiny observable decrease in the I/Pb ratio at the surface of region B near the counter electrode compared with the untreated control film ($\approx$1.91 and $\approx$1.97 at the region B of the perovskite films with and without pulsed e-field treatment, respectively). These observations indicate that the directed migration of mobile I⁻ ions along the opposite direction of the field at the surface of perovskite films, driven by a pulsed e-field, could stabilize iodine to inhibit evaporation.[32] That is to say, the pulsed e-field can suppress the formation of iodide vacancies, and fill iodide vacancies with the unanchored I⁻ ions moved in the perovskite films.[33,34]
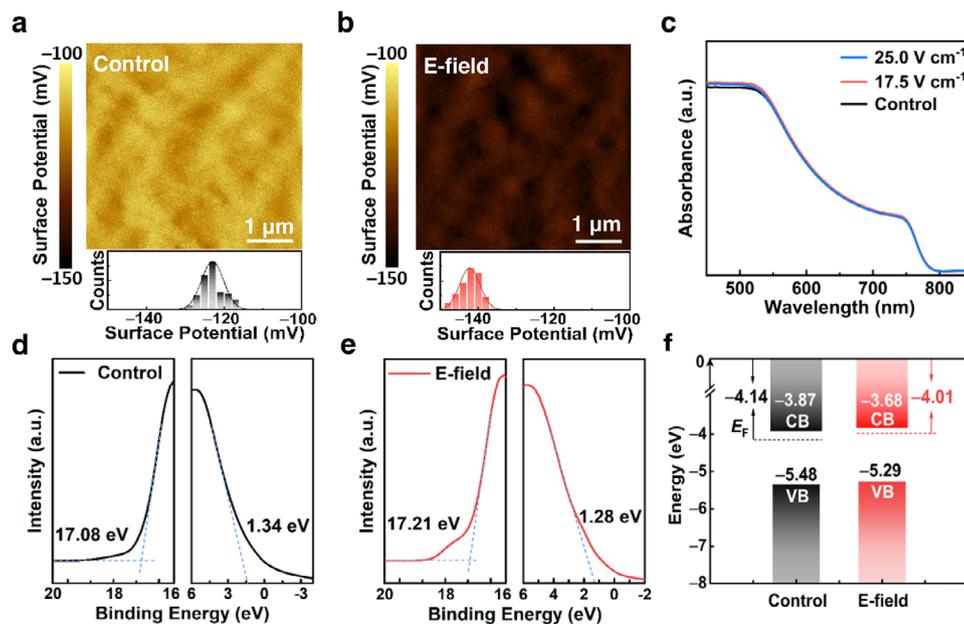
Furthermore, to investigate the effect of the applied pulsed e-field on the compositional distribution in the interior of the resultant perovskite film, the actual elemental mappings of I and Pb on the cross-sectional perovskite films were obtained from X-ray energy dispersive spectrometer (EDS). For the control perovskite film, the two selected regions (regions 1 and 2) near the two ends of the applied pulsed e-field direction had similar I/Pb ratios ($\approx$2.11 and $\approx$2.22 at the regions 1 and 2 of the control film, respectively) (Figure 2c). The EDS results showed a nearly uniform compositional distribution of I and Pb elements in the interior of the control perovskite film. The reason for the lower I/Pb ratio distributions of the control perovskite surface compared to the inner of the perovskite can be attributed to easy thermal evaporation of iodide species at the perovskite surface during the film-forming processing. Compared with the control perovskite film, the modified perovskite film after pulsed e-field treatment reached a relatively higher I/Pb ratio at the cross-sectional region 1 adjacent to the positive electrode, whereas the I/Pb ratio in the region 2 close to the negative electrode was characterized to be with a few minor change (Figure 2c). These results give a similar trend related to the I/Pb distribution in the interior of the perovskite film, as compared to that on the perovskite surface identified from XPS measurements. These observations further reveal the ability of pulsed e-field to immobilize iodine in perovskites during thermal annealing.

The distribution variations of the surficial and interior I/Pb ratios of the perovskites enabled by pulsed e-field treatment encouraged us to probe the distribution profiles of constituent species in the perovskite film. The line-scanning I-profiles of the pulsed e-field-treated perovskite film with EDS analysis exhibited higher intensity at the region close to the positive electrode (orange trace in Figure 2a) than that at the aligned region far from the same electrode (top panel of Figure 2d). In contrast, no significant change in intensity was characterized from the line-scanning profile of I distribution in the control film surface (bottom panel of Figure 2d). This suggests an existence of a lateral gradient distribution of I-related species in the perovskite film along the e-field direction after applying pulsed e-field on it under thermal annealing. In comparison of the surficial iodide distribution variations enabled by pulsed e-field, these were no obvious difference in the line-scanning profiles of Pb- and MA-related species at the selected regions along the field direction based on the identification of Pb and N element distributions, respectively, showing the negligible influence of Pb²⁺ and MA⁺ distribution in the properly modified perovskite by pulsed e-field (Figure S9, Supporting Information). These resulting profiles conform well to

the low activation energy for migration of free iodide ions along with the high activation energies for migration of Pb²⁺ and MA⁺ ions ($\approx$0.1 eV for I⁻, $\approx$0.5 eV for MA⁺, $\approx$0.8 eV for Pb²⁺).[35] Furthermore, Kelvin probe force microscopy (KPFM) measurements were used to investigate the influence of iodine distribution on the surface potential of the perovskite films. The line-scanning distribution of the surface potential difference of the pulsed e-field-treated perovskite film displayed a gradual increase of the surface potential from the positive electrode to the counter one compared with a random distribution of surface potential for the control perovskite film without pulsed e-field treatment (Figure S10, Supporting Information). The consequence of the increased surface potential profile is likely associated with a gradient distribution of electron-rich I⁻ ions in the perovskite film induced by the pulsed e-field. These characterization results have provided the evidences that a lateral gradient distributed I-ion species in perovskite film, regulated with a pulsed e-field, facilitates the formation of iodine-vacancy-less perovskite structures and high-quality films. Based on this understanding, the schematic diagram of ion migration and distribution regulated by a pulsed e-field as well as its effect on formation of the defect-less perovskite film are shown in Figure 2e. Initially, I-ion species exhibit strong orientation under the action of pulsed e-field during the thermal annealing of perovskite film and the directed migration of I ions, driven by a pulsed e-field, could reach a dynamic equilibrium against the driving force of the ionic concentration gradient. As a result, a lateral gradient distribution of I-ion species from the positive electrode to the counter one was achieved on the surface and throughout the interior of the perovskite film. Owing to the high activation energies required for migration of Pb²⁺- and MA⁺-related species, there is almost no significant effect toward Pb²⁺- and MA⁺-related species by applying pulsed e-field at 17.5 V cm⁻¹, as identified with the identical distribution of the Pb and N elements at two separated regions aligned in the direction in the modified perovskite film (Figure S9, Supporting Information). In addition, the varying inductive effect of the pulsed e-field can suppress the evaporation of iodide ions from perovskite film during thermal annealing to a certain extent. Furthermore, under the action of on-field migration and distribution of iodide ions within perovskite film following the application of a pulsed e-field, the iodide vacancies can be filled with the mobile I⁻ ions,[36] thus realizing the formation of iodide-vacancy-defect-less perovskite film with a highly crystalline and a preferential crystallographic orientation. It is noteworthy, for MA-based perovskite films treated using perpendicular-e-field-assisted annealing,[17] that ion polarization orientation in the perovskite films caused by ion migration with applied external e-field is emphasized to play an important role in effectively promoting charge separation and transport.

2.3. Improved Characteristics of Perovskite Films and Devices

The pulsed e-field can regulate the distribution of iodide species, thus affecting the surface energy of the perovskite film. The surface potential distribution of the perovskite films identified with KPFM is shown in **Figure 3a,b**. The e-field-treated perovskite film displayed the relatively low surface potential distribution compared with the e-field-free films, indicating that a Fermi level (E_F) is located closer to the conduction-band edge.[37]

**ADVANCED
SCIENCE NEWS**

www.advancedsciencenews.com

**small
methods**

www.small-methods.com

Figure 3. KPFM images (top panels) and the corresponding surface potential distributions (down panels) of a) control and b) pulsed e-field-treated perovskite films. c) UV–vis absorption spectra of perovskite films treated with and without pulsed e-field. UPS spectra of d) control and e) pulsed e-field-treated perovskite films, including secondary electron cut-off region (left panels) and near-Fermi edge region (right panels). f) Energy level scheme for the control and pulsed e-field-treated perovskite films extracted from UPS data.

Ultraviolet visible (UV–vis) absorption spectroscopy and ultra-violet photoelectron spectroscopy (UPS) were further conducted to reveal the optical properties and surface energy of the perovskite film. The UV–vis absorption spectra of the perovskite films with and without pulsed e-field treatment were shown in Figure 3c. The significantly improved optical absorbance of the e-field-treated film exhibited and the better light-harvesting capacity is predominantly due to the improved perovskite film crystallization and enlarged grain size.[38] This observation is beneficial for enhancing the short-circuit current density (J_{SC}) of the e-field-modified device. The Tauc diagram derived from UV–vis spectra indicates the bandgap (E_g) of the perovskite film is slightly decreased from 1.611 to 1.607 eV with the pulsed e-field treatment (Figure S11, Supporting Information). Additionally, the distribution of ionic species on perovskite surface influences the interfacial energy level. Figure 3d,e present the UPS spectra of the perovskite films treated with and without pulsed e-field, which revealed the cut-off energy ($E_{cut-off}$) and near-Fermi edge ($E_{F,edge}$) regions. The maximum valence band (E_V) of perovskite film was calculated using the equation $E_V = 21.22 - (E_{cut-off} - E_{F,edge})$, according to which the E_V values of the control and e-field-treated perovskite films were −5.48 and −5.29 eV, respectively. The corresponding work functions (WFs) of the control and e-field-treated perovskite films were determined at 4.14 and 4.01 eV, respectively. The minimum conductive band (E_C) energy levels were determined by the optical E_g calculated from the Tauc-plot methodology (Table S1, Supporting Information). The schematic energy band structure diagrams of the control and e-field-treated perovskite films were obtained (Figure 3f). After the pulsed e-field treatment, the E_F and E_C of the film increased by 0.13 and 0.19 eV, respectively, relative to the vacuum level (E_{VAC}), which indicates that the e-field-treated perovskite film exhibits more n-type

properties according to the shallower E_F. Additionally, compared with the E_V of the control perovskite film (−5.48 eV), that of the e-field-treated perovskite film is shallower to −5.29 eV. This clearly shows that pulsed e-field-treated perovskite film has an energy level matching with HTM of Spiro-OMeTAD (E_V = −5.22 eV),[39] beneficial for extracting charges from the perovskite to Spiro-OMeTAD and inhibiting non-radiative recombination in n-i-p planar PSCs.

Steady-state PL and time-resolved PL (TRPL) spectroscopies were employed to evaluate the charge-carrier dynamics in perovskite film. The pulsed e-field-treated perovskite film coated on the F-doped SnO$_2$ (FTO) substrate showed significantly enhanced PL intensities compared to the control film (**Figure 4a**), demonstrating a suppression of the non-radiative recombination in the perovskite film with increased grain sizes and a reduced occurrence of defects after pulsed e-field treatment. It is noteworthy that a slight red-shift was also observed in the PL peak maxima after pulsed e-field treatment (Figure S12, Supporting Information), potentially due to I-rich contribution on the perovskite surface.[40] The TRPL spectra also reflected the similar trend as the steady-state PL measurements (Figure 4b, the fitted parameters listed in Table S2, Supporting Information), where the perovskite film with pulsed e-field treatment on FTO substrate possessed a longer average carrier lifetime (τ_{ave}, ≈220.2 ns) compared with the control counterpart (≈138.5 ns). The prolonged τ_{ave} can be mainly attributed to increased film crystallinity and a reduced defect density in the perovskite film, thereby beneficial for suppressing the non-radiative recombination and facilitating the charge transport. Furthermore, temperature-dependent PL spectroscopic measurements were conducted to investigate the intrinsic photophysical properties of exciton in the perovskite film without and with pulsed e-field treatment. Different

**ADVANCED
SCIENCE NEWS**
www.advancedsciencenews.com

**small
methods**
www.small-methods.com
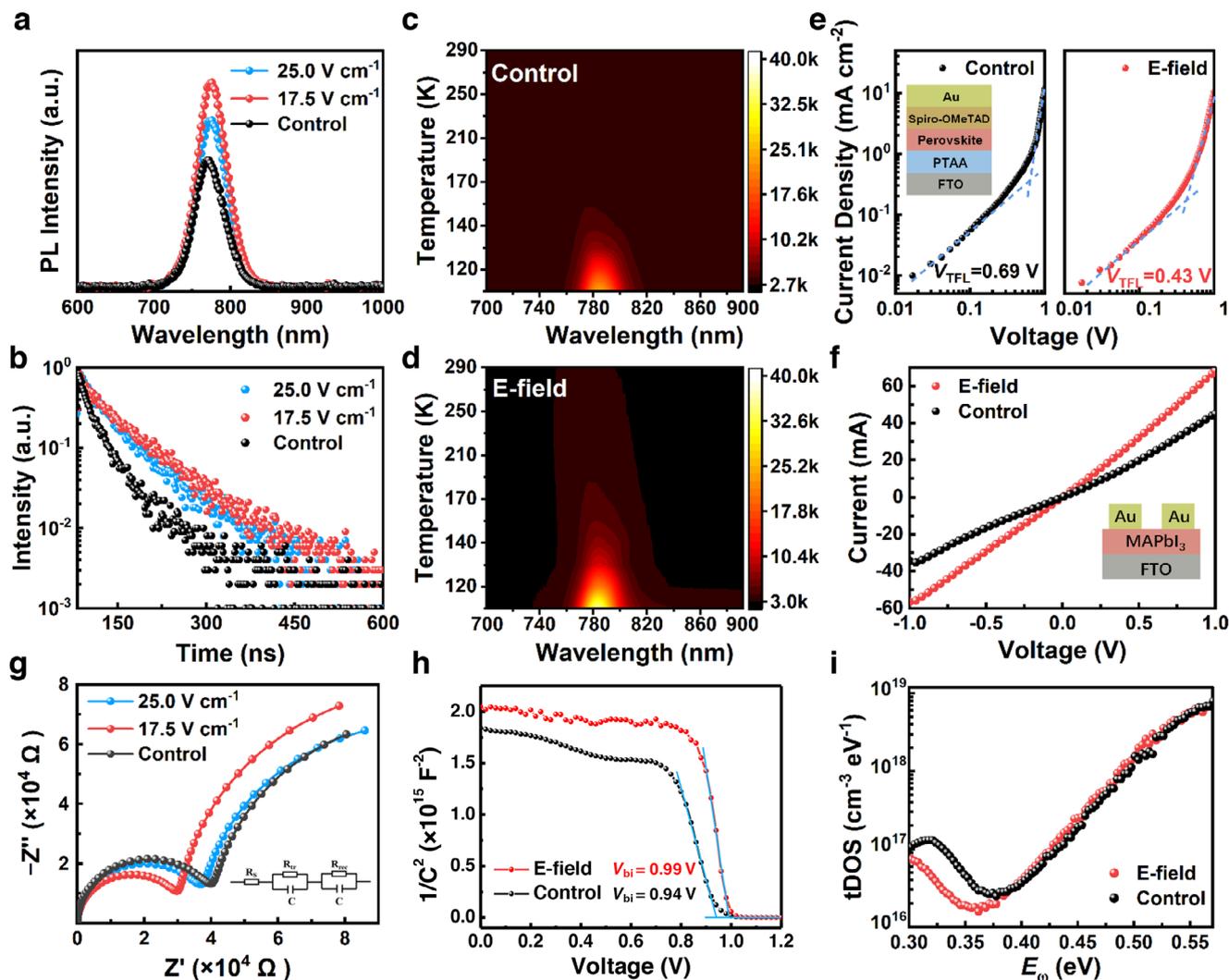
Figure 4. a) Steady-state and b) time-resolved PL spectra for control and pulsed e-field-treated perovskite films. Pseudo-colour maps of temperature-dependent PL spectra excited at 375 nm for c) control and d) pulsed e-field-treated perovskite films. e) Dark $J-V$ curves of hole-only devices prepared using control and pulsed e-field-treated perovskite films for SCLC analysis. f) The $I-V$ characteristic curves of FTO/perovskite/Au with control and pulsed e-field-treated perovskite films. g) Nyquist plots of the perovskite films without and with pulsed e-field treatment. The inset represents the equivalent circuit diagram. h) The Mott−Schottky plots of the devices with and without pulsed e-field treatment. i) The energy-dependent trap density of states (tDOS) of control and pulsed e-field-treated devices.

response of PL emissions from the 2D colour plots of PL intensity was observed for both perovskite films over a range of 80–290 K (Figure 4c,d). Both the control and e-field-treated perovskite films exhibited an increase in the emission intensity with the temperature during cooling (Figure S13a,b, Supporting Information). The increased PL intensity could attribute to the weakened lattice vibration at lower temperature, which leads to the reduction of thermally-activated non-radiative recombination in the perovskite film.[41,42] In addition, the exciton binding energy (E_b), which represents the exciton dissociation ability in perovskite film under light illumination, was calculated by fitting the temperature-dependent PL spectra (Figure S13c,d, Supporting Information). The E_b of the pulsed e-field-treated perovskite film was 40.90 meV, which is lower than that of the control film ($E_b = 48.75$ meV), indicating a more effective exciton dissociation in the resultant perovskite film with pulsed e-field treatment.

To directly evaluate the quality of the perovskite film prepared with pulsed e-field-assisted thermal annealing, the space-charge-limited current (SCLC) curves were recorded to quantitatively estimate the defect trap densities (N_{trap}) in perovskite film. The dark current density−voltage ($J-V$) curves of the hole-only devices are shown in Figure 4e, exhibiting the ohmic region at low bias and the trap-filled limited (TFL) region at intermediate bias. The ohmic and TFL regions were fitted linearly, and the voltage at the intersection of the two lines was determined as the trap-filling limited voltage (V_{TFL}) which is closely related to the N_{trap} according to the following equation: $N_{trap} = 2\varepsilon_r\varepsilon_0 V_{TFL}/eL^2$, where ε_r is the relative dielectric constant of the MAPbI$_3$ layer (28.8),[43] ε_0 denotes the vacuum permittivity (8.85×10^{-12} F m^{-1}), e represents the electron charge (1.6×10^{-19} C), and L denotes the thickness of the perovskite film ($\approx$400 nm from the cross-sectional SEM, Figure 1f,g). The device with pulsed

**ADVANCED
SCIENCE NEWS**

www.advancedsciencenews.com

**small
methods**

www.small-methods.com

e-field-treated perovskite film exhibited a V_{TFL} of 0.43 V (right panel of Figure 4e), which was lower than that of the control device (0.69 V, left panel of Figure 4e). Accordingly, the calculated N_{trap} values associated with hole traps were found to be 8.79×10^{15} and 5.47×10^{15} cm^{-3} for the control and pulsed e-field-treated perovskite films, respectively, similar to the values reported in previous works.[43,44] In addition, the electron trap densities for the control and e-field-treated perovskite films were characterized to be 8.27×10^{15} and 6.87×10^{15} cm^{-3}, respectively, after fitting the $J-V$ curves with electron-only devices (Figure S14, Supporting Information). These result confirmed that by treating with pulsed e-field, both hole and electron trap densities in the perovskite films could be decreased. Understandably, the reduced defect density in the e-field-treated perovskite film could reduce non-radiative recombination loss and extend the carrier lifetime in perovskite film, as evidenced by the result from the TRPL and PL measurements. These results attribute to the migration and distribution of iodide ions mediated with pulsed e-field, resulting in the suppressed iodine vacancy formation, along with the reduced I$^-$ interstitials.[45] To demonstrate the good charge-transfer ability of the pulsed e-field-treated perovskite film, the current-voltage ($I-V$) characteristic based on the structure of FTO/perovskite/Au was carried out under dark conditions.[46] Relative to the control device with the untreated perovskite film, the electrical conductivity (σ) of the counterpart with the e-field-treated film was significantly enhanced from 1.95×10^{-5} to 3.10×10^{-5} S cm^{-1} (Figure 4f). The results of conductivity demonstrate that the pulsed e-field-treated perovskite film is more conducive to charge transport and transfer.[47]

Electrochemical impedance spectroscopy (EIS) was performed to study the interfacial charge transport dynamics of the PSC devices. Figure 4g displayed the Nyquist polts of the control and e-field-based PSC devices applied bias voltage at 0.6 V in the darkness. Two different parts in the Nyquist plots could be observed: the arcs present in the high-frequency region are associated with the charge transport resistance (R_{tr}) at the interface with the perovskite and the incomplete semicircles present in the low-frequency region correlate to the charge recombination resistance (R_{rec}) of PSCs.[10] The EIS curves can be well fitted with the given equivalent circuit (inset of Figure 4g) and the corresponding values of R_{tr} and R_{rec} are summarized in Table S3 (Supporting Information). The pulsed e-field-treated device at 17.5 V cm^{-1} exhibited a low R_{tr}, and this can be attributed to the enhanced and oriented crystal grains in the perovskite films. Moreover, the R_{rec} of the e-field-treated device at 17.5 V cm^{-1} was calculated to be 2.3×10^5 Ω, considerably higher than that of e-field device at 25.0 V cm^{-1} (1.6×10^5 Ω) and control counterpart (7.7×10^4 Ω), signifying that nonradiative recombination losses can be effectively suppressed.[29] The built-in potential was characterized by Mott−Schottky analysis. Figure 4h revealed a more favorable flat band potential (V_{fb}) of 0.99 V in the pulsed e-field-treated PSC compared to 0.94 V in the control device.[48] The enhanced V_{fb} will be beneficial to the charge separating and transferring as well inhibiting the interface energy loss. Further, to quantify and visualize the defect energetic profiles in the perovskite film, thermal admittance spectroscopy (TAS) was performed to analyze the trap density of states (tDOS) within the relevant device (Figure 4i). The tDOS of the pulsed e-field-treated device was lower than that of

the control counterpart within the energy range below 0.37 eV, which showed the shallow traps were greatly eliminated. There results may be related to the suppression of shallow-level defects associated with iodide vacancies filled with unanchored I$^-$ interstitials. In contrast, the tDOS at deep level (>0.37 eV) in the e-field-treated perovskite film was barely changed compared to that of the untreated film, indicating that the Pb-related species, presented with high activation energies, were hardly involved in the migration induced by the applied pulsed e-field. The dramatically improved carrier mobility and lifetimes are probably ascribed to the reduced or diminished shallow-level defects associated with iodide. These results have shown that the introduction of pulsed e-field into thermal annealing can reduce the defect density, achieve the effective separation of exciton and facilitate the charge extraction and transport in the resultant perovskite film.

2.4. Photovoltaic Performance of Devices

The effects of a lateral gradient distribution of I-ion species in the perovskite film, which was mediated by the transverse pulsed e-field, on the device performance were evaluated by fabricating planar PSCs with the structure illustrated in Figure S15 (Supporting Information). The statistical distribution of photovoltaic parameters of the devices modified with varied intensities of pulsed e-field were compared systematically, as presented in Figure S16 (Supporting Information). The control devices exhibited an average PCE of $16.47 \pm 0.45\%$, an average J_{SC} of 21.86 ± 0.61 mA cm^{-2}, an average open-circuit voltage (V_{OC}) of 1.06 ± 0.04 V, and an average fill factor (FF) of $70.13 \pm 4.41\%$, which was increased to $19.00 \pm 0.31\%$ (PCE), 22.49 ± 0.28 mA cm^{-2} (J_{SC}), 1.07 ± 0.02 V (V_{OC}) and $77.35 \pm 1.17\%$ (FF), respectively, for the e-field-treated devices with the optimum intensity at 17.5 V cm^{-1} (Table S4, Supporting Information). The improved optical absorption intensity and charge transport at grain boundaries with larger grain size and less defects should be the main reasons for the increased J_{SC} in the thermal-annealed perovskite film with the pulsed e-field assistance.[49] The enhanced FF should be benefited from the ordered distribution of iodide species enabling better perovskite WF regulation, and migrated I$^-$ ions passivating the interfacial uncoordinated Pb^{2+} cations driven by pulsed e-field. It is noteworthy that a slightly improved reproducibility was observed for the modified devices with pulsed e-field treatment compared to the control devices, as supported by the statistical distribution diagram in Figure S16a (Supporting Information). The representative $J-V$ curves in reverse scan of the control and modified perovskite devices were shown in **Figure 5a**. The champion e-field-treated MAPbI$_3$-PSC delivered a J_{SC} of 22.48 mA cm^{-2}, a V_{OC} of 1.09 V, an FF of 78.37%, and a PCE of 19.32% (Table S4, note that the highest reported efficiency of PSCs with MAPbI$_3$ as the light-absorbing layer is 22.28%).[50] In contrast, the control counterpart achieved a J_{SC} of 21.86 mA cm^{-2}, a V_{OC} of 1.06 V, an FF of 74.71% and a PCE of 17.04%. Furthermore, the integrated photocurrent densities from the external quantum efficiency (EQE) spectra were calculated to be 21.65 and 22.32 mA cm^{-2} for the control and pulsed e-field-treated devices (Figure 5b), respectively, in accordance with the J_{SC} values extracted from the $J-V$ measurements. To assess the operation stability, the stabilized power

ADVANCED
SCIENCE NEWS

www.advancedsciencenews.com

small
methods

www.small-methods.com
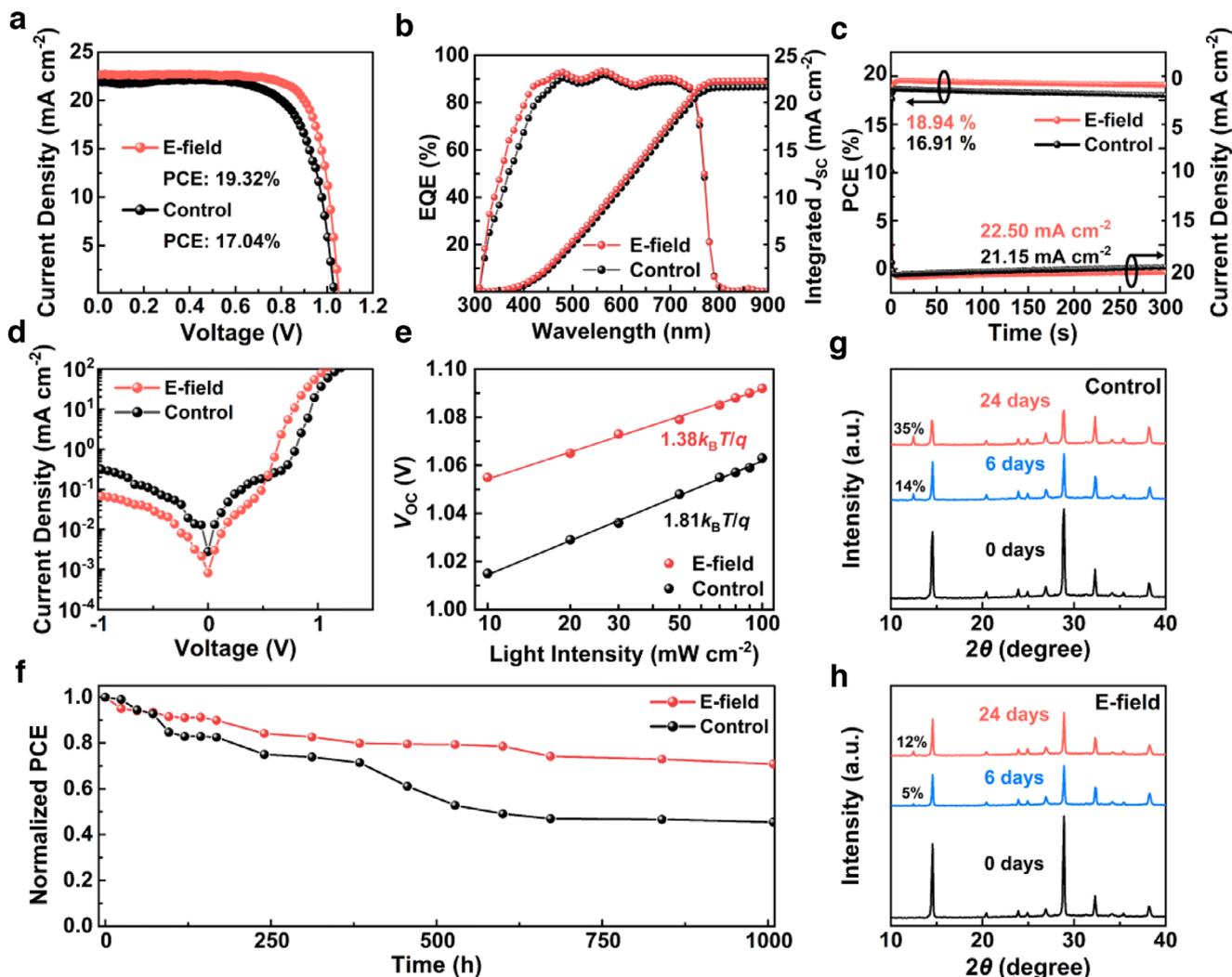
Figure 5. a) $J-V$ curves of the devices with and without pulsed e-field treatment. The active area of the device is $\approx$0.08 cm². b) EQE spectra and integrated J_{SC} of the corresponding devices. c) Stabilized photocurrent output and PCE measurements under maximum power point bias of the control and pulsed e-field-treated devices. d) Dark $J-V$ curves of the control and pulsed e-field-treated devices. e) V_{OC} versus light intensity of the control and pulsed e-field-treated devices. f) Storage stability tracking of the unencapsulated devices aged at ambient conditions with $\approx$20% RH and 20 $\pm$ 2 °C. XRD patterns of the g) control and h) pulsed e-field-treated perovskite films exposed to $\approx$20% RH and 20 $\pm$ 2 °C in ambient condition. The calculated ratios of the intensities of PbI$_2$ relative to the (110) plane are highlighted in panels g and h. The $J-V$ curves of devices without and with pulsed e-field treatment measured in both forward and reverse scan directions, along with the hysteresis index, were presented in Figure S17 (Supporting Information).

output (SPO) of the PSCs without and with pulsed e-field treatment were conducted (Figure 5c). The pulsed e-field-treated device, delivered the stabilized PCE of 18.94% and output current density of 22.50 mA cm⁻² for the test span of over 300 s, exhibited a more stable power output compared to the control device (16.91% of PCE, 21.15 mA cm⁻² of J_{SC}). To further evaluate the influence of the gradient distribution of iodine-related species on local device performance in pulsed e-field-treated perovskite films, the $J-V$ characteristics and SCLC analysis of sub-cells A and B, fabricated in regions aligned with the applied e-field direction, were conducted and compared (Figure S18 and Table S5, Supporting Information). The results revealed only minor performance variations between the two sub-cells, making it difficult to identify the gradient distribution of iodine-related species affecting local device performance.

To gain further insight into the behavior of charge transfer and carrier recombination, the dark $J-V$ measurements were conducted to analyze the leakage current of the device without and with pulsed e-field treatment (Figure 5d). It was found that the e-field-treated device possessed a relatively lower saturation current density J_0 compared with the control device, demonstrating that the photo-generated charge carriers effectively transfer through the transport layers with fewer shunt paths in the device. The reduced current leakage implies reduced shallower defects and less charge recombination in the pulsed e-field-treated device, which is in line with the PL results (Figure 4a,b).[49,51] Additionally, the impact of trap-assisted recombination on the device performance was assessed by tracking the seminatural logarithmic plots of V_{OC} as a function of light intensity (Figure 5e). The pulsed e-field-treated perovskite exhibited a lower slope of

1.38 $k_B T/q$, compared to a slope of 1.81 $k_B T/q$ for the control device. The much lower slope for the modified device demonstrates that the trap-assisted recombination is effectively suppressed by the treatment of pulsed e-field due to the reduced trap density as confirmed by the SCLC analysis.[25,52] The enhanced stability was also observed for the device with pulsed e-field treatment. As shown in Figure 5f, the PCE of the unencapsulated control device seriously decreased to ≈45% of its initial efficiency after exposure to an air atmosphere at RH ≈20% and 20 ± 2 °C for 1000 h. In contrast, the pulsed e-field-treated device maintained ≈70% of its original PCE over 1000 h, demonstrating a substantial improvement in the ambient stability. Table S6 (Supporting Information) demonstrated that the main parameter leading to the PCE dropping in e-field-treated PSCs was FF. The corresponding XRD patterns showed the PbI_2 peak gradually appeared after being exposed to ambient conditions, indicating film decomposition (Figure 5g,h). Compared with the control perovskite film appeared with an obvious increase of PbI_2 peak, the pulsed e-field-treated perovskite film showed significantly better resistance to the ambient environment based on the experimental indication of the reduced ratios of the intensities of PbI_2 relative to the (110) plane. These results demonstrate that the perovskite film treated with pulsed e-field during thermal annealing is effective for improving the operating stability of the PSCs, and the improved stability of the PSCs is attributed to the improved film quality, characterized by increased grain size, enhanced crystallinity, improved hydrophobicity, and diminished defect density in the perovskite film, resulting from the treatment with transverse pulsed e-field. Furthermore, this strategy was adaptable to the $FA_{0.85}MA_{0.1}Cs_{0.05}PbI_{2.85}Cl_{0.15}$ perovskites with mixed A-site cations and halides, delivering a notable PCE of 24.96% (24.10% PCE of PSC with the thermal-annealing-only film), thus demonstrating the potential effectiveness of regulation of ionic species distribution in perovskite film with pulsed e-field treatment for improving the performance of PSCs (Figure S19 and Table S7, Supporting Information; also see the detailed discussion of hysteresis effect in both $MAPbI_3$ and $FA_{0.85}MA_{0.1}Cs_{0.05}PbI_{2.85}Cl_{0.15}$ PSCs). On the basis of the above discussions, we further propose that an excess of iodide ions, not participated into the perovskite lattice, in the region near the positive electrode migrate and then self-fill the iodine vacancies generated in the operation to suppress the stress-driven structural collapse for alleviating the perovskite decomposition.

3. Conclusion

In this study, an additive-free approach has been explored to modulate the crystallization dynamics of the perovskite crystals. The transverse pulsed e-field, perpendicular to the perovskite surface, was applied for controlling the migration and distribution of the ionic species during the film formation. It was discovered that the incorporation of pulsed e-field leads to reduced loss of iodides during thermal annealing and suppressed formation of iodide vacancies. Moreover, a lateral gradient distribution of iodine-related species in the perovskite film was characterized, simultaneously demonstrating enhanced film crystallinity, improved carrier transport, extended carrier lifetimes, along with mitigated trap-state-related recombination in the resulting films. Iodides controlled with the pulsed e-field migrated and self-passivated

the iodide vacancies and interstitials, helping to eliminate defect-induced charge traps arising from shallow-level defects associated with iodide-related defects, thereby minimizing energy and charge losses. The resulting PSCs utilizing the additive-residual-free perovskite film achieved an enhanced efficiency, accompanied by significantly extended stability. This study has provided important insight regarding modulation of the migration and distribution of the halide-related species during perovskite film formation in advancing the efficiency and stability of PSCs.

Supporting Information

Supporting Information is available from the Wiley Online Library or from the author.

Conflict of Interest

The authors declare no conflict of interest.

Data Availability Statement

The data that support the findings of this study are available from the corresponding author upon reasonable request.

[1] Z. Zhang, L. Qiao, K. Meng, R. Long, G. Chen, P. Gao, *Chem. Soc. Rev.* **2023**, *52*, 163.

[2] J. Y. Kim, J.-W. Lee, H. S. Jung, H. Shin, N.-G. Park, *Chem. Rev.* **2020**, *120*, 7867.

[3] S. Li, Y. Jiang, J. Xu, D. Wang, Z. Ding, T. Zhu, B. Chen, Y. Yang, M. Wei, R. Guo, Y. Hou, Y. Chen, C. Sun, K. Wei, S. M. H. Qaid, H. Lu, H. Tan, D. Di, J. Chen, M. Grätzel, E. H. Sargent, M. Yuan, *Nature* **2024**, *635*, 82.

[4] H. Chen, C. Liu, J. Xu, A. Maxwell, W. Zhou, Y. Yang, Q. Zhou, A. S. Bati, H. Wan, Z. Wang, L. Zeng, J. Wang, P. Serles, Y. Liu, S. Teale, Y. Liu, M. I. Saidaminov, M. Li, N. Rolston, S. Hoogland, T. Filleter, M. G. Kanatzidis, B. Chen, Z. Ning, E. H. Sargent, *Science* **2024**, *384*, 189.

[5] J. Huang, Y. Yuan, Y. Shao, Y. Yan, *Nat. Rev. Mater.* **2017**, *2*, 17042.

[6] Q. Zhang, H. Huang, Y. Yang, M. Wang, S. Qu, Z. Lan, T. Jiang, Z. Wang, S. Du, Y. Lu, Y. Suo, P. Cui, M. Li, *Adv. Mater.* **2024**, *36*, 2410390.

[7] Z. Wu, S. Sang, J. Zheng, Q. Gao, B. Huang, F. Li, K. Sun, S. Chen, *Angew. Chem., Int. Ed.* **2024**, *63*, 202319170.

[8] M. Liu, J. Zhang, S. Qin, X. Miao, M. Yuan, Z. Liu, Y. Wang, Y. Feng, X. Jiang, R. Wu, Y. Yi, L. Meng, Y. Li, *J. Am. Chem. Soc.* **2024**, *146*, 32105.

[9] L. Xie, S. Du, J. Li, C. Liu, Z. Pu, X. Tong, J. Liu, Y. Wang, Y. Meng, M. Yang, W. Li, Z. Ge, *Energy Environ. Sci.* **2023**, *16*, 5423.

[10] J. Yang, W. Tang, R. Yuan, J. Chen, J. Wang, Y. Wu, W.-J. Yin, N. Yuan, J. Ding, W.-H. Zhang, *Chem. Sci.* **2021**, *12*, 2050.

[11] S. Wang, X.-Y. Gong, M.-X. Li, M.-H. Li, J.-S. Hu, *JACS Au* **2024**, *4*, 3400.

[12] T. Yang, Y. Yang, T. Niu, E. Zhao, N. Wu, S. Wang, X. Chen, S. Wang, Y. Wang, Y. Wu, Z. Zhang, C. Ma, Y. Gong, D. Liu, K. Zhao, *ACS Energy Lett.* **2025**, *10*, 427.

[13] S. Du, H. Huang, Z. Lan, P. Cui, L. Li, M. Wang, S. Qu, L. Yan, C. Sun, Y. Yang, X. Wang, M. Li, *Nat. Commun.* **2024**, *15*, 5223.

[14] Z. Xiong, X. Chen, B. Zhang, G. O. Odunmbaku, Z. Ou, B. Guo, K. Yang, Z. Kan, S. Lu, S. Chen, N. A. N. Ouedraogo, Y. Cho, C. Yang, J. Chen, K. Sun, *Adv. Mater.* **2022**, *34*, 2106118.

[15] J.-W. Lee, S. Tan, S. I. Seok, Y. Yang, N.-G. Park, *Science* **2022**, *375*, abj1186.

[16] C.-C. Zhang, S. Yuan, Y.-H. Lou, H. Okada, Z.-K. Wang, *Small* **2022**, *18*, 2107556.

[17] C.-C. Zhang, Z.-K. Wang, M. Li, Z.-Y. Liu, J.-E. Yang, Y.-G. Yang, X.-Y. Gao, H. Ma, *J. Mater. Chem. A* **2018**, *6*, 1161.

[18] C.-C. Zhang, Y.-H. Lou, M. Li, H. Okada, Z.-K. Wang, *Appl. Phys. Express* **2020**, *13*, 085503.

[19] M. Q. Wang, X. Zhang, S. Yan, N. A. N. Ouedraogo, Y. Zhang, H. Yan, C. B. Han, *Sustain. Energy Fuels* **2022**, *6*, 1121.

[20] Z. Cheng, D. Ding, J. Song, F. Liu, T. Wang, C. Hu, L. Ba, J. Wang, H. Liu, W. Shen, *Adv. Funct. Mater.* **2020**, *30*, 2004652.

[21] Y. Liu, N. Borodinov, L. Collins, M. Ahmadi, S. V. Kalinin, O. S. Ovchinnikova, A. V. Ievlev, *ACS Nano* **2021**, *15*, 9017.

[22] R. J. E. Westbrook, T. J. Macdonald, W. Xu, L. Lanzetta, J. M. Marin-Beloqui, T. M. Clarke, S. A. Haque, *J. Am. Chem. Soc.* **2021**, *143*, 12230.

[23] H. Wang, A. Guerrero, A. Bou, A. M. Al-Mayouf, J. Bisquert, *Energy Environ. Sci.* **2019**, *12*, 2054.

[24] Z. Liu, Z. Su, B. Yu, Y. Sun, J. Zhang, H. Yu, *ACS Appl. Mater. Interfaces* **2024**, *16*, 31218.

[25] Z. Song, Y. Gao, Y. Zou, H. Zhang, R. Wang, Y. Chen, Y. Chen, Y. Liu, *J. Am. Chem. Soc.* **2024**, *146*, 1657.

[26] S. Duan, Q. Sun, G. Liu, J. Deng, X. Meng, B. Shen, D. Hu, B. Kang, S. R. P. Silva, *ACS Appl. Mater. Interfaces* **2023**, *15*, 46483.

[27] O. S. Game, J. A. Smith, T. I. Alanazi, M. Wong-Stringer, V. Kumar, C. Rodenburg, N. J. Terrill, D. G. Lidzey, *J. Mater. Chem. A* **2020**, *8*, 10943.

[28] L. Yan, H. Huang, P. Cui, S. Du, Z. Lan, Y. Yang, S. Qu, X. Wang, Q. Zhang, B. Liu, X. Yue, X. Zhao, Y. Li, H. Li, J. Ji, M. Li, *Nat. Energy* **2023**, *8*, 1158.

[29] W. Zhang, J. Liu, W. Song, J. Shan, H. Guan, J. Zhou, Y. Meng, X. Tong, J. Zhu, M. Yang, Z. Ge, *Sci. Adv.* **2025**, *11*, adr2290.

[30] W.-Q. Wu, P. N. Rudd, Z. Ni, C. H. Van Brackle, H. Wei, Q. Wang, B. R. Ecker, Y. Gao, J. Huang, *J. Am. Chem. Soc.* **2020**, *142*, 3989.

[31] Y. Fang, T. Tian, M. Yang, Y. Tan, J.-X. Zhong, Y. Huang, X. Wang, J. Tao, S. Yang, C. Zou, S. Yang, Y. Peng, Q. Xue, W.-Q. Wu, *Adv. Funct. Mater.* **2023**, *33*, 2303674.

[32] D. W. deQuilettes, W. Zhang, V. M. Burlakov, D. J. Graham, T. Leijtens, A. Osherov, V. Bulović, H. J. Snaith, D. S. Ginger, S. D. Stranks, *Nat. Commun.* **2016**, *7*, 11683.

[33] L. Qiao, M. Guo, R. Long, *J. Phys. Chem. Lett.* **2024**, *15*, 1546.

[34] K. Zhang, Y. Wang, M. Tao, L. Guo, Y. Yang, J. Shao, Y. Zhang, F. Wang, Y. Song, *Adv. Mater.* **2023**, *35*, 2211593.

[35] J. M. Azpiroz, E. Mosconi, J. Bisquert, F. De Angelis, *Energy Environ. Sci.* **2015**, *8*, 2118.

[36] K. Huang, X. Feng, H. Li, C. Long, B. Liu, J. Shi, Q. Meng, K. Weber, T. Duong, J. Yang, *Adv. Sci.* **2022**, *9*, 2204163.

[37] L. Zhao, Q. Li, C.-H. Hou, S. Li, X. Yang, J. Wu, S. Zhang, Q. Hu, Y. Wang, Y. Zhang, Y. Jiang, S. Jia, J.-J. Shyue, T. P. Russell, Q. Gong, X. Hu, R. Zhu, *J. Am. Chem. Soc.* **2022**, *144*, 1700.

[38] P. Zhang, J. Xiong, W.-H. Chen, P. Du, L. Song, *Dalton Trans.* **2023**, *52*, 15974.

[39] Z. Shi, S. Liu, R. Luo, J. Ma, H. Tian, X. Wang, Z. Dong, X. Guo, J. Chen, J. Feng, C. Xiao, Y. Wu, W. Hu, Y. Hou, *J. Am. Chem. Soc.* **2025**, *147*, 1055.

[40] B. Wang, H. Li, Q. Dai, M. Zhang, Z. Zou, J.-L. Brédas, Z. Lin, *Angew. Chem., Int. Ed.* **2021**, *60*, 17664.

[41] M. Chen, X. Dong, Y. Xin, Y. Gao, Q. Fu, R. Wang, Z. Xu, Y. Chen, Y. Liu, *Angew. Chem., Int. Ed.* **2024**, *63*, 202315943.

[42] P. Wang, B. Wang, Y. Liu, L. Li, H. Zhao, Y. Chen, J. Li, S. Liu, K. Zhao, *Angew. Chem., Int. Ed.* **2020**, *59*, 23100.

[43] T. Das, A. Kumar, S. Rani, A. Guchhait, D. S. Ghosh, *Adv. Eng. Mater.* **2024**, *26*, 2302078.

[44] Z. Li, J. Cao, X. Yang, D. Cao, Y. Li, L. Zhao, S. Wang, *ACS Appl. Mater. Interfaces* **2025**, *17*, 22860.

[45] L. Qiao, W.-H. Fang, R. Long, O. V. Prezhdo, *Angew. Chem., Int. Ed.* **2020**, *59*, 4684.

[46] J. Li, J. Duan, C. Zhang, Z. Qi, Y. Liu, X. Duan, Y. Liu, J. Dou, Q. Guo, B. He, Y. Zhao, P. Yang, Q. Tang, *eScience* **2025**, *5*, 100372.

[47] M. Wu, H. Wang, Y. Li, R. Chen, H. Zhou, S. Yang, D. Xu, K. Li, Z. An, S. Liu, Z. Liu, *Angew. Chem., Int. Ed.* **2023**, *62*, 202313472.

[48] S. Xiong, Z. Hou, S. Zou, X. Lu, J. Yang, T. Hao, Z. Zhou, J. Xu, Y. Zeng, W. Xiao, W. Dong, D. Li, X. Wang, Z. Hu, L. Sun, Y. Wu, X. Liu, L. Ding, Z. Sun, M. Fahlman, Q. Bao, *Joule* **2021**, *5*, 467.

[49] B. Liu, H. Bi, D. He, L. Bai, W. Wang, H. Yuan, Q. Song, P. Su, Z. Zang, T. Zhou, J. Chen, *ACS Energy Lett.* **2021**, *6*, 2526.

[50] K. Wang, C. Wu, Y. Hou, D. Yang, T. Ye, J. Yoon, M. Sanghadasa, S. Priya, *Energy Environ. Sci.* **2020**, *13*, 3412.

[51] Y. Xu, X. Guo, Z. Lin, Q. Wang, J. Su, J. Zhang, Y. Hao, K. Yang, J. Chang, *Angew. Chem., Int. Ed.* **2023**, *62*, 202306229.

[52] D. Shi, V. Adinolfi, R. Comin, M. Yuan, E. Alarousu, A. Buin, Y. Chen, S. Hoogland, A. Rothenberger, K. Katsiev, Y. Losovyj, X. Zhang, P. A. Dowben, O. F. Mohammed, E. H. Sargent, O. M. Bakr, *Science* **2015**, *347*, 519.